Journal of the Mechanical Behaviour of Biomedical Materials 2010
doi:10.1016/j.jmbbm.2009.12.004

Mixed-mode stress intensity factors for kink cracks with finite kink length loaded in tension and bending

– Application to dentin and enamel -

Sabine Bechtle[1], Theo Fett[2], Gabriele Rizzi[3], Stefan Habelitz[4], Gerold A. Schneider[1]

[1]*Institute of Advanced Ceramics, Hamburg University of Technology, Denickestr. 15, D-21073 Hamburg, Germany*
[2]*Institute for Ceramics in Mechanical Engineering, University of Karlsruhe (TH), Haid und Neu Straße 7, D-76131 Karlsruhe, Germany*
[3]*Institute for Materials Research II, Forschungszentrum Karlsruhe, Hermann von Helmholtz Platz 1, D-76021 Karlsruhe, Germany*
[4]*Department of Preventive and Restorative Dental Sciences, University of California, San Francisco, CA 94143, USA*

Abstract. Fracture toughness resistance curves describe a material's resistance against crack propagation. These curves are often used to characterize biomaterials like bone, nacre or dentin as these materials commonly exhibit a pronounced increase in fracture toughness with crack extension due to co-acting mechanisms as crack bridging, crack deflection and microcracking. The knowledge of appropriate stress intensity factors which depend on sample and crack geometry is essential for determining these curves. For the dental biomaterials enamel and dentin it was observed that under bending and tensile loading crack propagation occurs under certain constant angles to the initial notch direction during testing procedures used for fracture resistance curves determination. For this special crack geometry (kink crack of finite length in a finite body) appropriate geometric function solutions are missing. Hence, we present in this study new mixed-mode stress intensity factors for kink cracks with finite kink length within samples of finite dimensions for two loading cases (tension and bending) which were derived from a combination of mixed-mode stress intensity factors of kink cracks with infinitely small kinks and of slant cracks. These results were further applied to determine fracture resistance curves of enamel and dentin by testing single edge notched bending (SENB) specimens. It was found that kink cracks with finite kink length exhibit identical stress fields as slant cracks as soon as the kink length exceeds 0,15 times the initial straight crack or notch length. The usage of stress intensity factor solutions for infinitely small kink cracks for the determination of dentin fracture resistance curves (as was done by other researchers) leads to an overestimation of dentin's fracture resistance of up to 30%.

Key words: fracture resistance curves, stress intensity factor, kink cracks, enamel, dentin

1. Introduction

Single edge notched bending (SENB) and compact tension (CT) specimens are quite commonly used to determine fracture toughness values of materials as a function of crack extension Δa. In metallic or ceramic materials, cracks tend to propagate within initial notch direction under pure mode I loading. For this general case, stress intensity factor solutions are available (Fett and Munz, 1997; Murakami, 1986). However, in biomaterials like for example the dental materials enamel and dentin it could be observed that cracks grow away from the initial notch under a certain constant angle φ (Bajaj and Arola, 2009; Koester et al., 2008). As a consequence of oblique crack propagation, mixed-mode stress conditions are induced at the crack tip – more precisely, a combination of mode I (tensile) and mode II (in-plane shear) loading. A schematic drawing of this crack geometry can be seen in Figure 1a. We call these cracks "kink cracks with finite kink length in a finite body" – i.e. the dimensions of the kinking crack Δa reach the same magnitude as the notch a_0 and the sample dimensions.

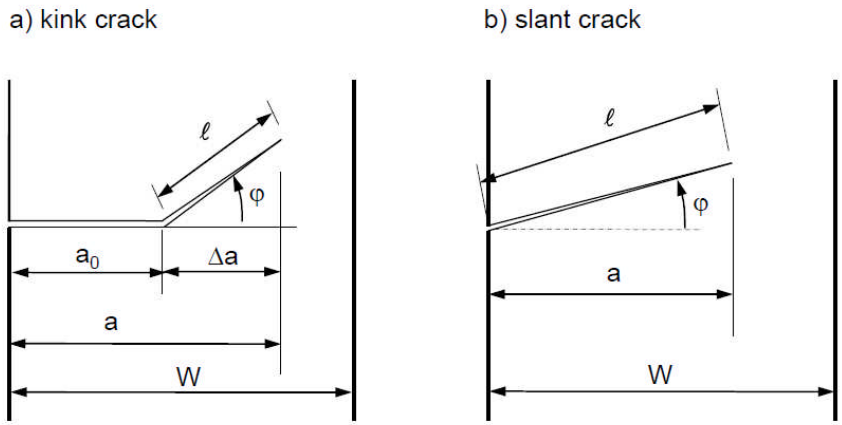

Figure 1: Schematic drawings of the crack geometries relevant for this study. a) kink crack: cracks emerge from the starter notch at a certain constant angle φ. For a kink crack with infinitely small kinks the condition Δa → 0 (i.e. $\ell \rightarrow 0$) has to be fulfilled. For a kink crack with finite kink length, Δa reaches dimensions comparable to the ones of a_0 and W. b) slant crack: notch and emerging crack have to lie on the same linear slope.

For this special type of crack geometry, no geometric function solutions are available in the literature. The handbook of Murakami for instance (Murakami, 1986) reports geometric function solutions for kink cracks with finite kink length. Nevertheless, these solutions are valid for semi-infinite bodies only and thus, are not appropriate for application to sample geometries of finite dimensions. For finitely dimensioned bending bars geometric functions are available for slant cracks, where the notch and crack lie on the same linear slope (see Figure 1b; Munz and Fett, 2001) and for kink cracks with infinitely small kink (Figure 1a, $\ell \rightarrow 0$). For the latter ones the solution of Cotterell and Rice (1980) is most often used to compute the stress intensities of the infinitely small kink crack from the singular stress field of the straight crack. However, to the authors' knowledge, there are no geometric functions available for kink cracks of finite kink length within finite bodies. Thus, a geometric function for this special crack geometry was derived in this study for two loading conditions (tension and bending).

The derived solutions were furthermore used to determine fracture resistance curves for enamel and dentin. These curves were compared with literature data for enamel and dentin to

illustrate the needs of the new geometric function solution presented here and to discuss the applicability of the newly derived solution to the dental biomaterials enamel and dentin (see section 3).

2. Stress Intensity Factors

The mixed-mode stress intensity factors for kink cracks with finite kink length were derived from a combination of the mixed-mode stress intensity factors of kink cracks with infinitely small kink and of slant cracks. Thus, solutions for the latter two crack geometries loaded to tension and bending are presented in sections 2.1 and 2.2, followed by the solution for kink cracks with finite kink length in section 2.3. The particular geometries of kink and slant cracks are illustrated in Figure 1.

2.1 Kink cracks in finite bodies with infinitely small kink length loaded in tension and pure bending

The stress intensity factors at the tip of a kink of length ℓ can be written for $\ell << a_0$ as

$$K_{\mathrm{I}}(\ell) = K_{\mathrm{I}}(a_0)\, g_{11} + b_1 T\sqrt{\ell} \tag{1}$$

$$K_{\mathrm{II}}(\ell) = K_{\mathrm{I}}(a_0)\, g_{21} + b_2 T\sqrt{\ell} \tag{2}$$

where $K_I(a_0)$ is the stress intensity factor for the initial straight crack a_0 and T is the fracture mechanics T-stress term representing the first regular term of the stress field at a crack tip (Cotterell and Rice, 1980). The angular functions are given by

$$g_{11} = \cos^3(\varphi/2) \tag{3}$$

$$g_{21} = \sin(\varphi/2)\cos^2(\varphi/2) \tag{4}$$

$$b_1 = \sqrt{\frac{8}{\pi}}\sin^2\varphi \tag{5}$$

$$b_2 = -\sqrt{\frac{8}{\pi}}\sin\varphi\cos\varphi \tag{6}$$

The limit case of the infinitely small kink of projected length $\Delta a \to 0$ (i.e. $\ell \to 0$) at the tip of the initial straight crack of depth a_o (total projection of crack length: $a = a_0 + \Delta a$, see Figure 1a) is considered. The mixed-mode stress intensity factors for this case are given by

$$K_{\mathrm{I,II,kink}}(\alpha, a) = \sigma F_{\mathrm{I,II,kink}}(\alpha)\sqrt{a\pi} \tag{7}$$

with the geometric functions for tension and bending, respectively:

$$F^{t,b}_{I,kink}(\alpha) = F_{t,b}(\alpha)\cdot g_{11} = F_{t,b}(\alpha)\cdot\cos^3(\varphi/2) \tag{8}$$

$$F^{t,b}_{II,kink}(\alpha) = F_{t,b}(\alpha)\cdot g_{21} = F_{t,b}(\alpha)\sin(\varphi/2)\cos^2(\varphi/2) \tag{9}$$

with $F_t(\alpha)$ and $F_b(\alpha)$ being the solutions for geometric functions of a straight crack normal to the free front and side surface loaded in tension ($F_t(\alpha)$) or bending ($F_b(\alpha)$) according to

$$F_t(\alpha) = \frac{1.1215}{(1-\alpha)^{3/2}}\left[1 - 0.23566(1-\alpha) + \frac{1}{150}(1-\alpha)^2 + 3\alpha^2(1-\alpha)^7 + 0.229\exp(-7.52\frac{\alpha}{1-\alpha})\right] \quad (10)$$

and

$$F_b(\alpha) = \frac{1.1215}{(1-\alpha)^{3/2}}\left[\frac{5}{8} - \frac{5}{12}\alpha + \frac{1}{8}\alpha^2 + 5\alpha^2(1-\alpha)^6 + \frac{3}{8}\exp(-6.1342\frac{\alpha}{1-\alpha})\right] \quad (11)$$

with $\alpha = a/W$ (Fett and Munz, 1997).

2.2 Slant cracks in finite bodies loaded in tension and pure bending

A slant edge crack in a finite plate of width W under an angle φ to the x-axis is illustrated in Figure 1b. The mixed-mode stress intensity factors K_I and K_{II} for such a crack may be defined via the true crack length ℓ and the ratio $\lambda = \ell/W$ by

$$K_{I,II}(\ell, \lambda) = \sigma\, Y_{I,II,\,slant}(\lambda)\sqrt{\pi \cdot \ell} \quad (12)$$

or by use of the crack length projection $a = \ell \cos(\varphi)$ and $\alpha = a/W$ via

$$K_{I,II}(a, \alpha) = \sigma\, F_{I,II,\,slant}(\alpha)\sqrt{\pi\, a} \quad (13)$$

with, trivially

$$Y_{I,II}(\lambda) = F_{I,II,slant}(\alpha)\sqrt{\cos\varphi} \quad (14)$$

for φ being in radian and $Y_{I,II,\,slant}(\lambda)$, $F_{I,II,\,slant}(\alpha)$ being the geometric functions depending on true crack length ℓ ($\lambda = \ell/W$) and crack length projection a ($\alpha = a/W$), respectively.

2.2.1 Slant cracks in finite bodies loaded in tension

Geometric functions for a slant crack under tensile load are given in Figure 2. The circles represent numerical data from a stress intensity factor handbook (Fett and Munz, 1997), diamond squares are results obtained by Finite Element Analysis conducted by the authors.

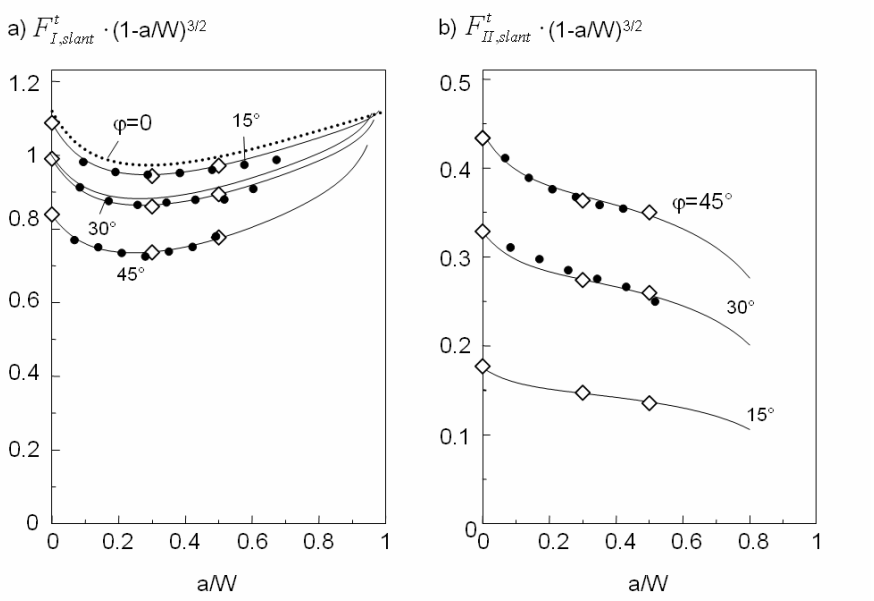

Figure 2: Geometric functions $F^t_{I,II,slant} \cdot (1-a/W)^{3/2}$ for slant cracks under tensile loading as defined in equations 13 and 14 for tilt angles φ = 15°, 30° and 45°. a) geometric function for mode I, b) geometric function for mode II; Squares: Finite Element results, circles: numerical data from (Fett and Munz, 1997), solid lines: fit relation according to equations (17) and (18).

Equations (1)-(6) describing stress intensity factors at the tip of a kink crack with infinitely small kink length were used for the construction of an appropriate fit-formula for the mode I and II geometric functions for slant cracks based on the assumption that the relations for kink cracks with small kink length also reflect some main features of long kink cracks, i.e. slant cracks as limit case for $a_0 \rightarrow 0$.

In order to fulfil this limit case automatically and to match the numerical results from literature and the own FE-results, a relation of the type given in equations (1) and (2) was used with fit functions $f(\varphi, \ell/W)$ depending on the kink angle φ and the relative crack depth ℓ/W according to

$$F_{\mathrm{I}}(\ell) = F_{\mathrm{I}}(a_0)\, g_{11} + f_1(\varphi, \ell/W) b_1 T \sqrt{\ell} \tag{15}$$

$$F_{\mathrm{II}}(\ell) = F_{\mathrm{II}}(a_0)\, g_{21} + f_2(\varphi, \ell/W) b_2 T \sqrt{\ell} \tag{16}$$

The effect of ℓ/W on the functions f_1 and f_2 was found to be negligible. With $a_0 \rightarrow 0$ and $\ell = a/\cos\varphi$ it follows that $F_I(a_0)$ and $F_{II}(a_0)$ vanish and only the second part of equations (15) and (16) remain. Finally the fit-functions are

$$F^t_{I,slant}(\alpha) = F_t(\alpha)[\cos^3(\tfrac{1}{2}\varphi) + 0.1504\beta \sin^2\varphi / \sqrt{\cos\varphi}] \tag{17}$$

$$F^t_{II,slant}(\alpha) = F_t(\alpha)[\cos^2(\tfrac{1}{2}\varphi)\sin(\tfrac{1}{2}\varphi) - 0.2348\beta \sin\varphi \sqrt{\cos\varphi}] \tag{18}$$

with the dimensionless representation of T by the biaxiality ratio β proposed by Leevers and Radon (1982)

$$\beta = \frac{T\sqrt{\pi a}}{K_{\mathrm{I}}} = \frac{T}{\sigma_t F_t} \tag{19}$$

with σ_t being the externally applied remote tensile stress.
The function $F_t(\alpha)$ denotes the tensile solution for a straight crack normal to the free side surface (see equation (10)).

The biaxiality ratio β for tension reads (Fett, 2008)

$$\beta = \frac{-0.469 + 0.1456\,\alpha + 1.3394\,\alpha^2 + 0.4369\,\alpha^3 - 2.1025\,\alpha^4 + 1.0726\,\alpha^5}{\sqrt{1-\alpha}} \tag{20}$$

with α = a/W.

2.2.2 Slant cracks in finite bodies loaded in pure bending

Geometric functions for a slant crack under pure bending are given in Figure 3. The circles represent the numerical data from (Fett and Munz, 1997) obtained by application of the weight function technique. Our Finite Element results are introduced by the diamond squares. Analogues to the tensile solution (previous section) a fit relation is proposed for the mode-I and mode-II geometric functions

$$F^b_{I,slant}(\alpha) = F_b(\alpha)[\cos^3(\tfrac{1}{2}\varphi) + 0.17845\beta\sin^2\varphi/\sqrt{\cos\varphi}] \tag{21}$$

$$F^b_{II,slant}(\alpha) = F_b(\alpha)[\cos^2(\tfrac{1}{2}\varphi)\sin(\tfrac{1}{2}\varphi) - 0.2182\,\beta\sin\varphi\sqrt{\cos\varphi}] \tag{22}$$

where $F_b(\alpha)$ is the bending solution for a straight crack normal to the free side surface (see equation (11)) and the biaxiality ratio for bending (Fett, 2008)

$$\beta = \frac{-0.469 + 1.2825\alpha + 0.6543\alpha^2 - 1.2415\alpha^3 + 0.07568\,\alpha^4}{\sqrt{1-\alpha}} \tag{23}$$

The fit functions are shown in Figure 3 by the solid lines.

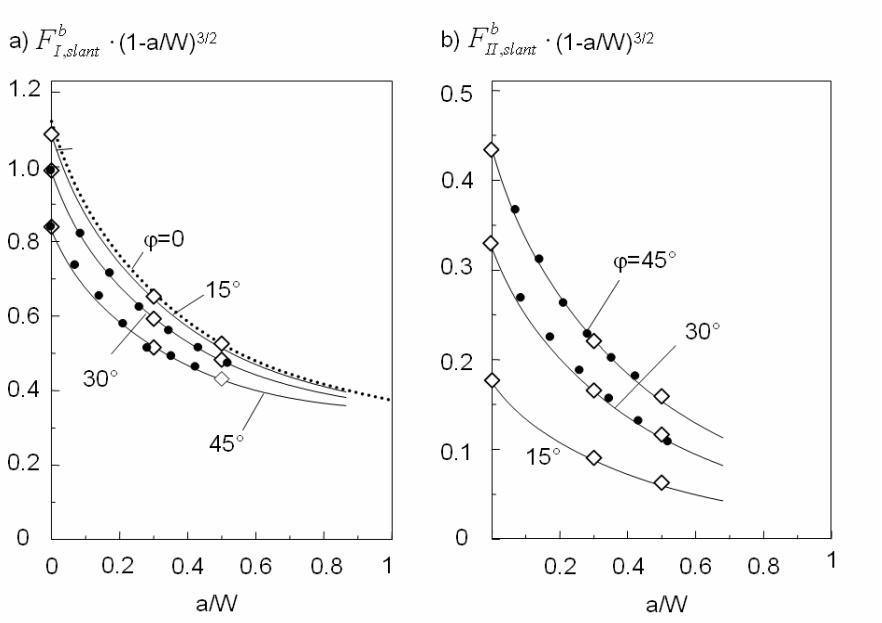

Figure 3: Geometric functions $F^b_{I,II,slant} \cdot (1-a/W)^{3/2}$ for slant cracks under bending loading as defined in equations (13) and (14) for tilt angles 15°, 30°, 45°. a) geometric function for mode I, b) geometric function for mode II; Symbols: circles represent numerical data from (Fett and Munz 1997), squares: Finite Element computation, solid lines: fit relation according to equations (21) and (22).

2.3 Kink cracks in finite bodies with finite kink length loaded in tension and bending

For $\varphi < 50°$, a simple estimation of F_I and F_{II} from the limit values for $\Delta a/a \to 0$ (infinitely small kink at a crack normal to the surface) and $\Delta a/a \to 1$ (slant crack) derived before is possible by interpolation of the solutions for the slant crack and the normal crack with infinitely short kink according to

$$F^{t,b}_{I,II} = F^{t,b}_{I,II,kink} + (F^{t,b}_{I,II,slant} - F^{t,b}_{I,II,kink}) \tanh[\sqrt{\mu_{I,II} \frac{\Delta a}{a}}] \qquad (24)$$

with $\mu_I = 25$ and $\mu_{II} = 12$ obtained by application of a least-squares fitting procedure to results by Finite Element Analysis and other numerical solutions (Noda et al., 1992; Fett and Rizzi, 2005). $F^{t,b}_{I,II,kink}$ and $F^{t,b}_{I,II,slant}$ are either the solutions for bending (equations 8 and 9 with 11 for $F^b_{I,II,kink}$ and equations 21, 22 for $F^b_{I,II,slant}$) or tension (equations 8 and 9 with 10 for $F^t_{I,II,kink}$ and equations 17, 18 for $F^t_{I,II,slant}$) according to the load applied.

This interpolation relation is applied in Figure 4 to literature data (Noda et al., 1992; Fett and Rizzi, 2005) for $\varphi = 30°$ and 45°. From these diagrams it can be concluded that for $\Delta a > 0{,}15a$ a kink crack with finite kink length already exhibits the same mixed-mode stress intensity

factors as the slant crack. In this context it has to be mentioned that for $a << W$ (edge-cracked half space) the bending and tensile solutions trivially coincide.

Finite Element results are plotted in Figure 5 for tension and bending loading. These data confirm the result of Figure 4 that already for $\Delta a > 0{,}15a$ kink cracks with finite crack length and slant cracks exhibit identical stress intensity factors.

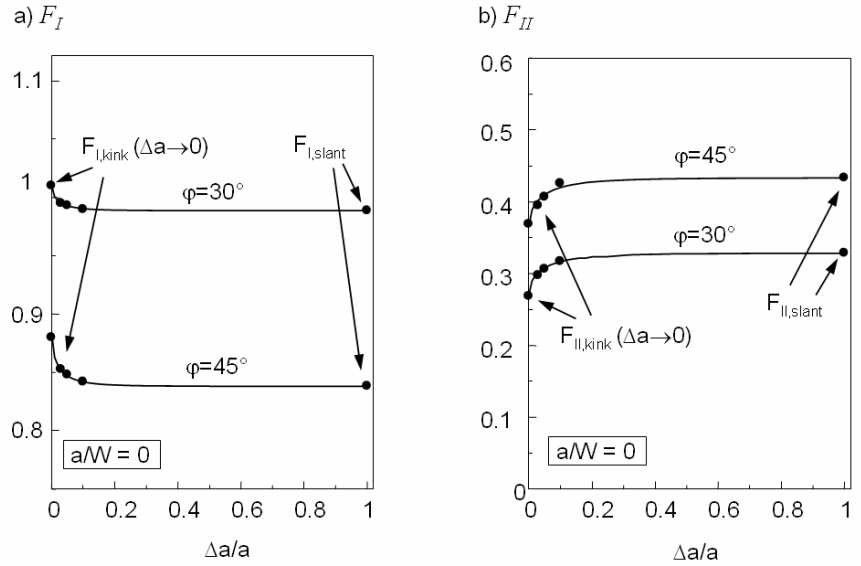

Figure 4: Geometric functions $F_{I,II}$ for kink cracks for $a/W = 0$ (half space ($W \to \infty$) – bending and tensile solutions coincide); circles: data from Noda et al. (1992) and Fett and Rizzi (2005); solid lines: interpolation according to equation (24).

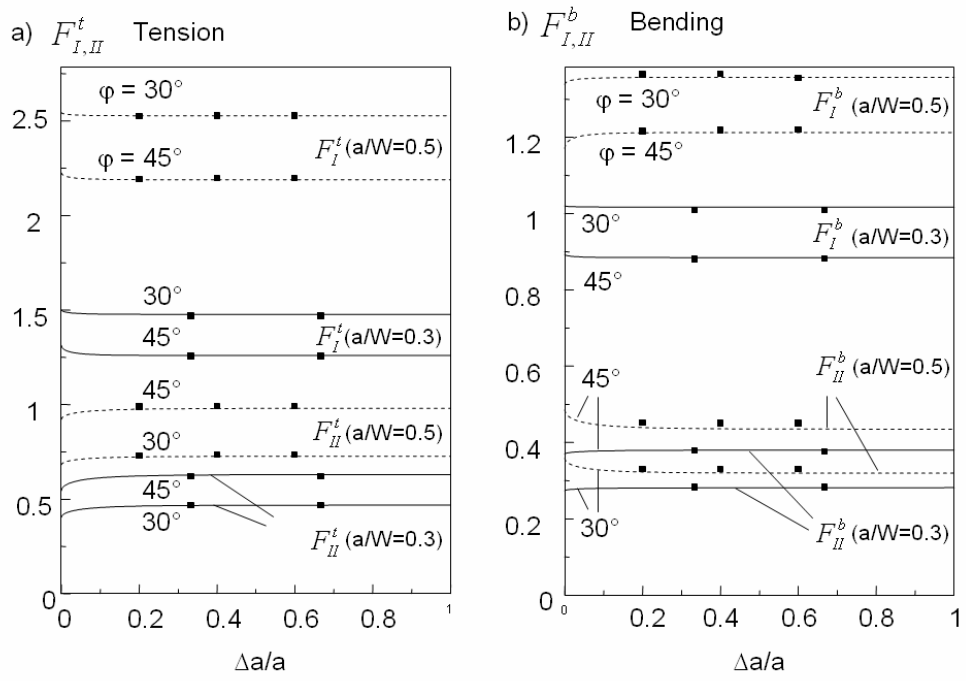

Figure 5: Geometric functions $F^{t,b}_{I,II}$ for kink cracks with finite kink length in a finite bar under tension and bending loading; squares: Finite Element results, solid lines: interpolation according to equation (24) for a/W = 0,3, dashed lines: interpolation according to equation (24) for a/W = 0,5.

2.4 Application of geometric function solutions for kink cracks with finite kink length to 3- and 4-point bending

The bending solution of equation (24) for kink cracks in finite bodies with finite kink length is valid for samples loaded in pure bending, hence for samples solely exposed to a bending moment. In practice, bending experiments are conducted by using 3- or 4-point bending setups where shear forces are introduced additionally to a bending moment. However, in the case of 4-pont bending, the deviation of the geometric function from the solution for pure bending is negligible (less than 0,2 %) if the ratio of bar width W to the inner roller span S_i is less than one third (W/S_i < 1/3) as can be seen from the analysis of Nisitani and Mori (1985). Thus, geometric function solutions for pure bending can directly be applied to experimental data obtained by 4-point bending as long as the condition W/S_i < 1/3 is fulfilled.
In the case of 3-point bending (the type of experimental setup used in this study), the differences between geometric function solutions for 3-point bending and pure bending are small as can be seen in Tada's handbook (Tada et al., 1986) especially for large aspect ratios S/W (loading span S / sample width W). The geometric function obtained for pure bending can thus be modified for S/W = 7 (the aspect ratio used in this study) by the factor $C(\alpha) = \frac{F_b(3PB)}{F_b(4PB)} \cong 0{,}95 + 0{,}05 \cdot \alpha$ (i.e. the ratio of the geometric function of an SENB bar loaded in 3-point bending to the one of a SENB bar tested in 4-point bending) with $\alpha = a/W$.

This approximation is based on curves given in Tada's handbook (Tada et al., 1986) for 3-point bending and pure bending and the assumption that differences in geometric function solutions for 4-point and pure bending can be neglected.

With this approximation, stress intensities for kink cracks with finite kink length in 3-point bending bars can be calculated according to

$$K_{I,II}(a,\alpha) = \sigma\sqrt{\pi a}\cdot F^{b}_{I,II}(\alpha)\cdot C(\alpha) \tag{26}$$

with σ being the externally applied bending stress, *a* being the corresponding crack length as indicated in Figure 1a, and $F^{b}_{I,II}(\alpha)$ being the geometric function solution for pure bending (equation (24)).

3. Application to Biomaterials

Dentin is the most abundant material in human teeth and is physically located between the exterior enamel layer and the interior pulp chamber. It is composed of ~ 47 vol% hydroxyapatite crystallites (HAP), ~ 20 vol% water and ~ 33 vol% proteins, mainly collagen (Lussi, 2006). The collagen fibrils are infiltrated and impregnated with nanometre-scaled HAP crystallites (5 nm in thickness) (Kinney et al., 2001) and form a network like structure with the fibril long axes lying perpendicular to the dentinal tubules. Dentin tubules are cylindrically shaped channels (1-2 μm in diameter) that span the entire dentin layer from the pulp chamber to the dentinoenamel junction (DEJ), the interface between enamel and dentin (Ten Cate, 2003). They are surrounded by a highly mineralized cuff of peritubular dentin and contain nerve fibres and cell processes emanating from the pulp chamber (Ten Cate, 2003).
Enamel is the hardest tissue in the human body and covers the dental crown. It is composed of ~ 85 vol% hydroxyapatite crystals, ~ 12 vol% water and ~ 3 vol% organic matrix (Lussi, 2006). On the microstructural level enamel is composed of HAP - fibre bundles, the enamel rods (about 5 μm in diameter), that run from the DEJ to approximately 6-12 μm below the tooth surface (Gray et al., 1995). The enamel rods are embedded within a fibrous matrix, the interrod region. Both enamel rods and matrix consist of HAP crystallites and proteins: within the rods, the HAP crystallites are at least 100 μm long (Gray et al., 1995) with their long axes being parallel to the rod axes whereas in the matrix the crystallites are inclined at certain angles to adjacent rod axes. Within the interface between rods and interrod region water and proteins are assumed to accumulated due to lower HAP density in that area (Maas and Dumont, 1999). Thus, rod boundaries appear as distinct protein-rich structures called 'rod sheaths'. The entire enamel layer can be divided into outer (close to the tooth surface) and inner enamel (close to the DEJ) (Ten Cate, 2003); within the outer enamel layer the enamel rods are aligned very straight and parallel to each other whereas they are decussated or interwoven in the inner enamel region.
Figure 6 displays the microstructure of bovine enamel and dentin as bovine incisors were used in this study. It has been previously pointed out that human and bovine enamel / dentin exhibit a very similar microstructure (Oesterle et al., 1998; Sanches et al., 2009; Schilke et al., 2000) and it can also be seen from Figure 6 that all basic microstructural features described previously for human teeth can be found in the bovine teeth cross sections as well. Additionally, it was observed by the authors in previous experiments that the enamel layer of bovine incisors can also be divided into inner and outer enamel with decussated and straight enamel rod arrangement, respectively, analogues to human enamel.

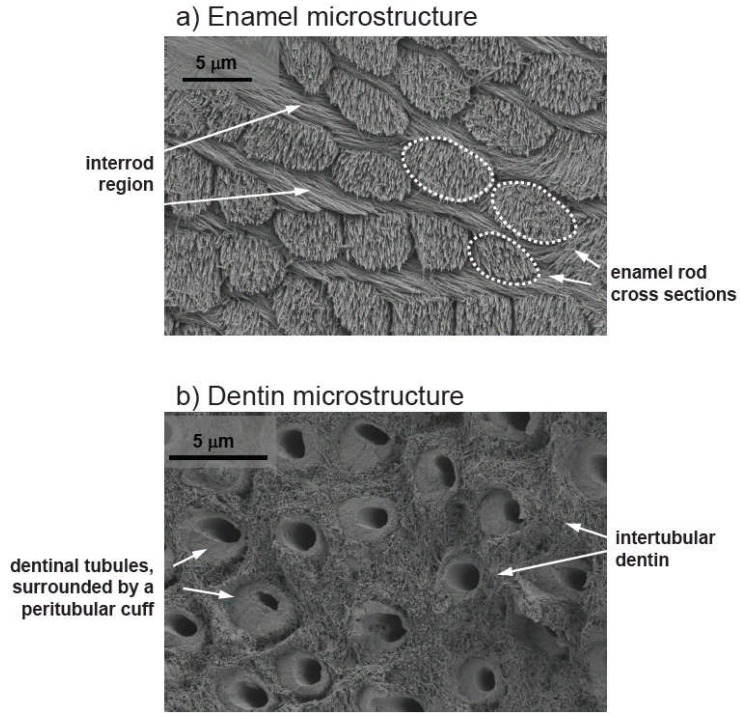

Figure 6: Microstructure of bovine enamel (a) and dentin (b). To make the enamel microstructure visible, a polished enamel cross section was etched with 35% phosphoric acid for 20 seconds. The enamel rod cross sections are very well visible. Each single rod consists of bundles of parallel aligned HAP-crystallite-fibers. The interrod region also consists of HAP-fibers but they are inclined at a certain angle to enamel rod long axes. In non-etched enamel, single HAP crystallites as well as rods are impregnated with proteins. The dentin cross section was created by fracturing a dentin bar perpendicular to the dentinal tubules. The tubules are surrounded by a highly mineralized peritubular cuff. The intertubular dentin is built by a network of collagen fibers reinforced by HAP crystallites.

For both materials – enamel and dentin – fracture toughness resistance curves were already published (Bajaj and Arola, 2009; Koester et al., 2008). In both materials, crack propagation was observed to occur under a certain constant angle to initial notch direction. In the case of dentin (Koester et al., 2008), the authors chose a stress intensity factor solution for the geometry of a kink crack with infinitely small kink length, although the limits of this solution ($\ell << a_0$) were exceeded. Though calculating mixed-mode stress intensities K_I and K_{II} they did not show these values separately but calculated an effective fracture toughness $K_{eff} = (K_I^2 + K_{II}^2)^{1/2}$. This approach is appropriate for isotropic materials with elliptical K_I-K_{II}-failure criteria, but due to the complex hierarchical structure of dentin it might be possible that the failure criterion for dentin differs hereof.
In the case of enamel (Bajaj and Arola, 2009), the authors tried to force cracks on straight paths in the initial notch direction by introducing a back channel on the back side of the samples, but according to the micrographs shown, cracks still propagated under a certain constant angle to initial notch direction. Only a mode I fracture toughness is presented though mixed-mode stress conditions were induced at the crack tip due to oblique crack propagation.

To embrace oblique crack propagation and associated mixed-mode stress conditions in enamel and dentin, we determined mode I and mode II fracture resistance curves by testing SENB samples prepared out of bovine incisors and applying the previously derived formulas

for data evaluation. Bovine incisors were used instead of human teeth due to their larger amount of especially enamel and the flatness of the enamel layer which enabled bending bar preparation (see Figure 7). As mentioned previously the microstructure of bovine and human teeth is very similar as well as it was shown for human and bovine dentin that they exhibit very similar mechanical properties (Sano et al., 1994). Bending bars (~ 1x1x10 mm^3) were cut from bovine incisors as indicated in Figure 7. All bending bar surfaces were polished up to 1200 grit SiC paper. The surface on which crack propagation was monitored was additionally polished up to 0,05 μm diamond suspension. Samples were notched to roughly 30-40% of their total width using razor blades irrigated with 6 μm diamond suspension. Notches were further sharpened to ~ 20 μm notch diameter using razor blades irrigated with 1 μm diamond suspension. Notches (see Figure 7) were oriented in enamel and dentin as was done in the studies of Bajaj and Arola (2009) and Koester et al. (2008): within enamel, the notch front was placed roughly perpendicular to enamel rod long axes in the outer enamel layer so that crack propagation was initiated parallel to the rods in the outer enamel. Crack propagation occurred towards the DEJ. Due to the large notches (30-40% of sample width) crack propagation mainly occurred within the region of inner enamel.
Within dentin the notch front was chosen to be roughly parallel to dentinal tubule long axes. However, it is never possible to align dentinal tubules or enamel rods of the outer enamel region exactly with respect to sample surfaces and thus, rods and tubules are indicated slightly inclined in the sketches shown in Figure 7.

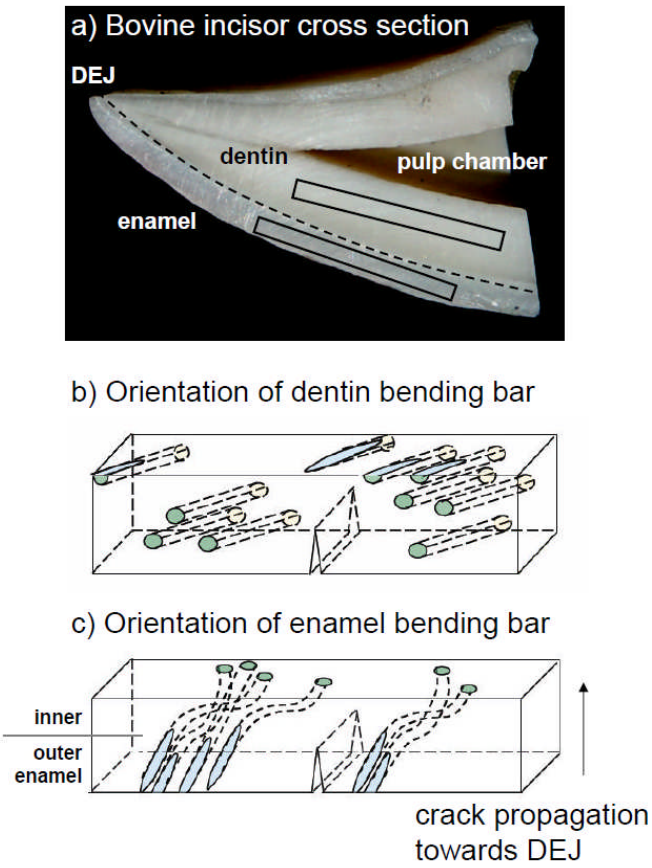

Figure 7: Bovine incisor cross section (a) and sample orientation (b, c). Samples were cut from bovine incisors at the sites indicated in (a). Orientation of the notch front in dentin samples was chosen to be roughly parallel to dentinal tubule long axis. However, as it is never possible to align the dentin tubules exactly with respect to sample surfaces, they are indicated here as inclined cylinders. In enamel samples (b) notch fronts were placed roughly perpendicular to the enamel rod long axes of the outer enamel layer. Due to the notch depth, crack extension occurred basically within the inner enamel region, where rods are decussated (indicated by meandering cylinders). Crack propagation occurred towards the DEJ.

Samples were coated with a 5 nm gold layer after polishing and notching for better crack visibility during mechanical testing. Samples were stored within HBSS (Hank's Balanced Salt Solution, Invitrogen, USA) to avoid drying-out and were always irrigated with fluid during sample preparation. After finishing sample preparation and before mechanical testing, samples were stored for at least 12-24h within HBSS. Mechanical testing was done in ambient air after wiping the samples using a custom-made bending device equipped with a quartz load sensor (quartz dynamic load cell 9212, Kistler Instrumente GmbH) of high sensitivity (-11,3 pC/N) to measure the force acting on the sample and an optical microscope with 400x magnification for visual crack length determination. The load within the loading range applied (0-10 N) was measured with 5% accuracy; the crack length was determined accurate to 3 µm. A 3-point bending cell with a loading span S of 7 mm was used. The lower support was fixed whereas the displacement of the upper support (and thus the load acting on the sample) could be changed manually. For a more detailed description of the device used see Jelitto et al.,

2007. Testing of each sample was completed within 30 minutes after removing samples from HBSS. Stress intensities were calculated due to equation (26) and were plotted as a function of Δa. For calculations, it was assumed that inelastic / plastic processes are restricted to a small region around crack tips in both enamel and dentin and hence, small scale yielding prevails in these two materials.

Figure 8 shows micrographs of tested samples. Crack propagation occurred under ~ 30° to initial notch direction within dentin, under ~ 45° in enamel.

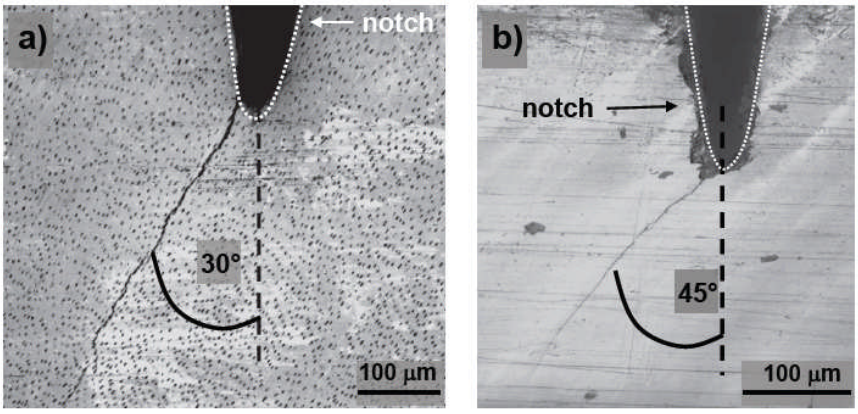

Figure 8: Crack profiles of tested samples. Crack propagation occurred under 30° in dentin (a) and under 45° in enamel (b).

Within enamel, the oblique crack propagation potentially was caused by oblique arrangement of groups of enamel rods having the same orientation within the inner enamel region. Such groups of rods are visible under optical microscopes as dark and light alternating bands, so-called "Hunter-Schreger-bands" (Ten Cate, 2003). Within one band, enamel rods have the same orientation, between adjacent bands orientation changes. Hunter-Schreger bands only exist within the inner (decussated) enamel – in the outer enamel, all rods are alligned parallel, having the same orientation. As can be seen in Figure 9, crack propagation occurred within such a Hunter-Schreger band and thus we assume that oblique Hunter-Schreger band orientation forced cracks on their oblique paths.

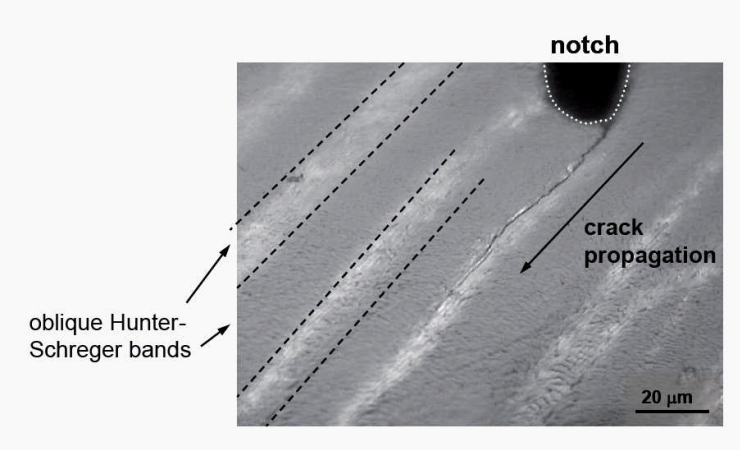

Figure 9: Oblique crack propagation in enamel was likely caused by Hunter-Schreger band orientation. Hunter-Schreger bands can be seen in this optical micrograph as alternating dark and light bands. Crack propagation occurred within one of these bands within which a bundle or enamel rods is arranged in the same orientation. Between adjacent Hunter-Schreger bands rod orientation changes.

Oblique crack propagation in dentin could not be attributed to microstructure that easily. Crack propagation occurred perpendicular to tubule long axes and thus, could not be influenced by oblique tubules analogues to oblique Hunter-Schreger bands. At this point we can only speculate what forced cracks on oblique paths within dentin. Maybe, a protein-shearing mechanism is involved, as intertubular dentin consists of HAP-reinforced collagen-fibrils which might favourably deform and fracture under shear.

There was no significant difference in crack orientation or crack path on the sample front and the sample back side of enamel and dentin samples – thus, it was assumed for further calculations that crack profiles had a rather straight profile throughout the sample thickness (see also Bechtle et al., 2009).

The determined mode I and mode II fracture resistance curves are displayed in Figure 10. Because of the lack of a known fracture criterion for enamel and dentin under mixed-mode loading we suggest to present K_I and K_{II} separately without calculating an effective stress intensity value. In further studies, these missing fracture criteria should be determined for the two materials by varying the mode I/mode II loading ratio, for example in asymmetric bending tests.
Additionally, the role of K_{II} for crack propagation has to be further investigated: within enamel, K_{II} is about one third of K_I and rises with crack extension whereas in dentin, K_{II} is almost constant (K_{II} ~ 0,4 MPa*$m^{1/2}$). Though being much smaller than K_I, K_{II} might be an important driving force for crack extension as this component was induced solely by internal material structure and not due to external loading conditions.
Toughening (the increase in K_I and K_{II} with crack extension) was attributed to microcracking, uncracked ligament bridging, protein bridging, and crack deflection in previous studies (Bajaj and Arola, 2009; Bechtle et al., 2009; Koester et al., 2008).

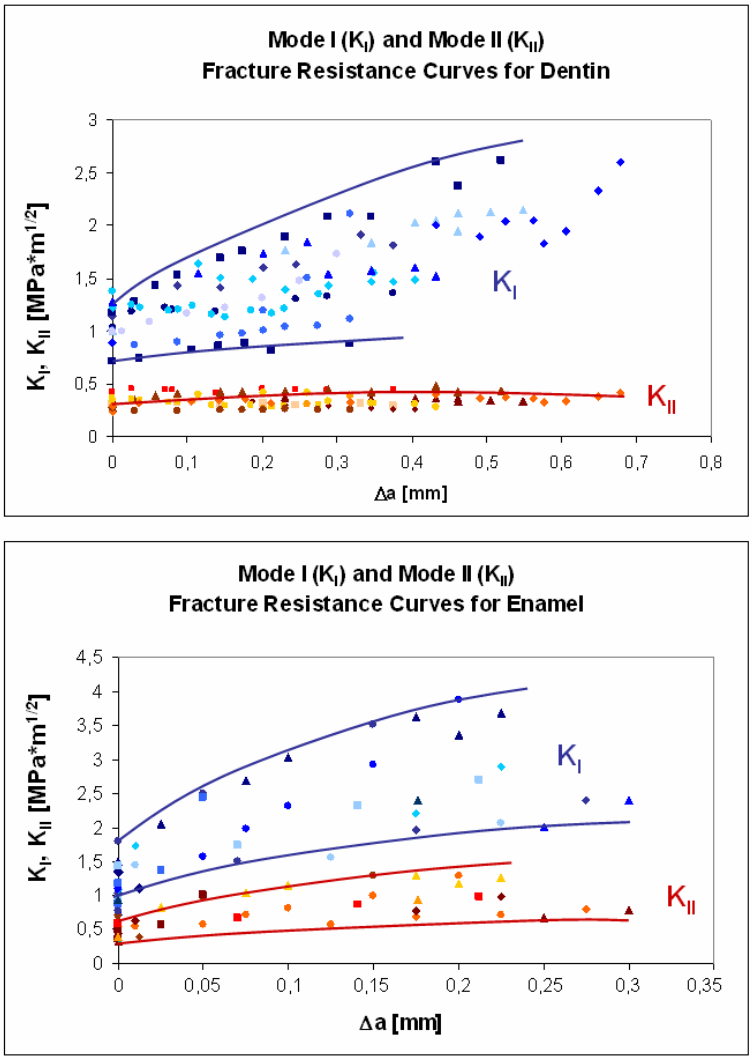

Figure 10: Mode I and mode II fracture resistance curves for dentin (a) and enamel (b). The mode I (K_I – coloured in blue tones) and mode II (K_{II} – coloured in red tones) values are plotted as a function of crack extension Δa. Each data point type represents a separate sample (dentin: n = 13, enamel: n = 14). K_{II} is about one third of K_I within enamel and rises with crack extension. K_{II} in dentin is almost constant (K_{II} ~ 0,4 MPa*m$^{1/2}$). The solid curves represent the upper and lower limits of the measured samples.

The initial K_I values for enamel lie between 0,6 and 1,8 MPa*m$^{1/2}$ at the beginning of crack propagation ($\Delta a \rightarrow 0$ mm), within dentin the initial values range from 0,7 to 1,4 MPa*m$^{1/2}$. Some amount of this large scatter is likely caused by a notch radius effect: as cracks for K_I, K_{II} determination were initiated directly away from the notch without introducing a sharp fatigue pre-crack, initial K_I, K_{II} values might be a bit overestimated as a result of finite notch radii (Fett, 2005). As notch radii vary among samples (notches were placed and sharpened manually), contribution of the notch radius effect on the determined initial K_I, K_{II} values varies as well. However, after some microns of crack propagation, notch effects vanish (for Δa > 1,5 notch radius, ~ 15 – 20 µm) (Fett, 2005). The scatter of the values still present at crack extensions larger than that might be attributed to natural variations always present in biomaterials (like for example variations in mineral amount and density between individual teeth or size and amount of pre-existing microcracks that can coalesce during crack propagation).

Figure 11 displays the K_I, K_{II} data for dentin determined in this study by testing SENB samples and using the evaluation according to equation (26) (solid data points). For comparison with the procedure used by Koester et al. (2008), the original data for the bovine dentin tested in this study was additionally evaluated by using the same equations as Koester et al. (hollow data points) but without applying the last formula (calculating K_{eff} out of K_I and K_{II}). For a clear arrangement only the data points for the two samples building the lower and the upper limit of the K_I, K_{II} ranges are shown. The regions in which all the other data points are located are shaded.

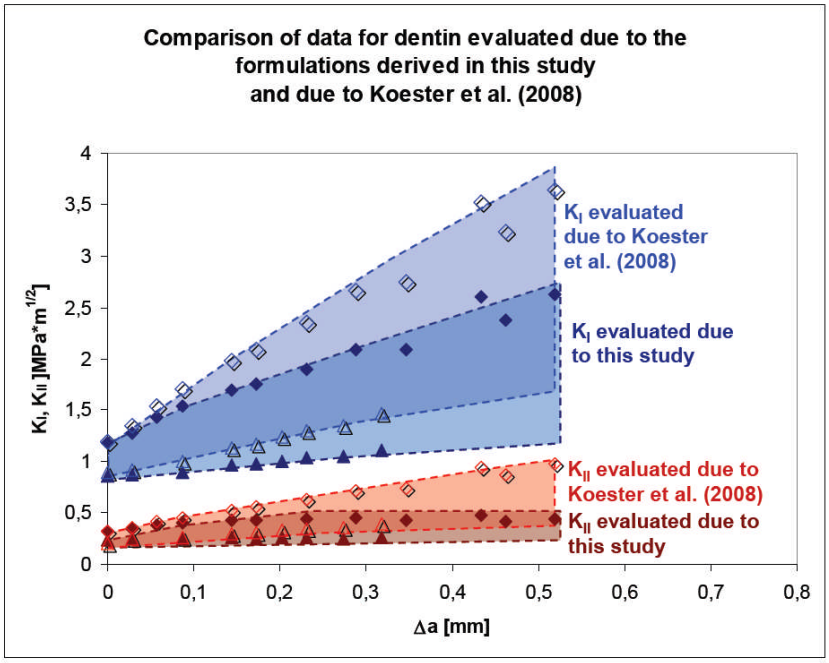

Figure 11: The original data for dentin were evaluated as described in this study and additionally with the same equations as used by Koester et al. (2008) for a comparison of the two different geometric function solutions. As can be seen, the application of the method used by Koester et al. (2008) results in an overestimation of K_I and K_{II} for long cracks. For small amounts of crack extension ($\Delta a \rightarrow 0$ mm, i.e. $\ell \rightarrow 0$) where Koester's method is valid, the two solutions coincide.

As can be seen from Figure 11 the values calculated using the method as done by Koester et al. (2008) results in overestimated K_I, K_{II} values for large Δa (up to 30%). For $\Delta a \rightarrow 0$ mm (the region where the method according to Koester et al. (2008) is valid as kinks are of infinitely small length), data of both evaluation methods coincide.

The range of data points for the bovine dentin tested here and evaluated according to Koester et al. (2008) fits very well to the data presented by Koester et al. (2008) for human dentin.

A direct comparison between the data for enamel from this study with the data for enamel derived from Bajaj and Arola, 2009 is not that easily possible as the comparison between the dentin data of this study and results from Koester et al. (2008). The dentin data in this and Koester et al.'s (2008) study were derived with same sample geometry (SENB) and notch configuration (manually inserted notch of finite width) whereas Baja and Arola (2009) used a

CT specimen with a sharp fatigue pre-crack to determine their fracture resistance curves. Bajaj and Arola's (2009) initial K_I values range from 0,5 to 0,8 MPa*$m^{1/2}$ – these values are lower and show a smaller amount of scattering than the K_I values determined in this study which likely can be attributed to the fine starting crack used by Bajaj and Arola (2009) eliminating any notch effects. However, after 1 mm crack extension within the inner enamel region, the values presented by Bajaj and Arola (2009) are around 2,5 MPa*$m^{1/2}$ which is even far lower than the values around 4 MPa*$m^{1/2}$ determined in this study after 0,25 mm crack extension in the inner enamel region. This discrepancy might arise from the different specimen geometries used. According to Fett et al. (2000) the K values determined with CT specimens for large cracks are significantly lower than values determined with SENB samples. As the values for $\Delta a \rightarrow 0$ mm show a much lower discrepancy than the K_I values after some amount of crack extension this explanation seems reasonable. Fett et al. (2000) recommend in general to evaluate the upper and lower limits of K for a certain material – thus one could state (assuming that human and bovine enamel exhibit very similar mechanical properties analogues to dentin) that the values presented for enamel in this study represent the upper and Bajaj and Arola's (2009) values represent the lower K_I limits for enamel. However, the advantage of our evaluation is the determination of both K_I and K_{II} – Bajaj neglected the K_{II} term although that term was present due to oblique crack propagation.

4. Conclusion

In this study, we present new geometric function solutions for kink cracks with finite kink length in finite bodies. It was found that for kink lengths larger than 0,15 times the initial straight crack or notch length, the stress intensity factors for kink cracks and slant cracks are identical.

Fracture resistance curves for the dental biomaterials enamel and dentin were determined by testing SENB samples and evaluating the obtained data using the newly derived geometric functions. It is suggested that as long as the detailed fracture criteria for enamel and dentin are not known, mode I and mode II stress intensity values are plotted separately. The influence of the mode II component (which was induced solely due to internal material structure and not due to external loading conditions) on the fracture process has to be investigated in further studies as well as the fracture criteria for enamel and dentin should be determined.

Until now - because of the lack of a solution for finite kink cracks in bending bars - the fracture toughness of dentin was evaluated with a solution of geometric functions for infinitely small kinks. This results in an overestimation of the fracture resistance of dentin up to 30%.

Acknowledgement

This paper is published in **Journal of the Mechanical Behaviour of Biomedical Materials 2010**
doi:10.1016/j.jmbbm.2009.12.004
Special thanks go to Dipl-Ing Anja Borchert, Hamburg University of Technology for technical support and scientific discussions.

References

Bajaj, D., Arola, D.D., 2009. On the R-curve behaviour of human tooth enamel. Biomaterials 30, 4037-46.

Bechtle, S., Habelitz, S., Fett, T., Klocke, A., Schneider, G.A., 2009. The fracture behaviour of dental enamel. Biomaterials, in press, doi: 10.1016/j.biomaterials.2009.09.050.

Cotterell, B., Rice, R.C., 1980. Some remarks on elastic crack-tip stress fields. Int. J. Fract. 16, 155-169.

Fett, T., Munz, D., 1997. Stress intensity factors and weight functions, Computational Mechanics Publications, Southampton.

Fett, T., Munz, D., Geraghty, R.D., 2000. White KW. Influence of specimen geometry and relative crack size on the R-curve. Eng. Fract. Mech. 66, 375-386.

Fett, T., Rizzi, G., 2004. T-stress solutions determined by finite element computations, Report FZKA 6937, Forschungszentrum Karlsruhe, Karlsruhe.

Fett, T., Rizzi, G., 2005. Weight functions for stress intensity factors and T-stress for oblique cracks in a half-space. Int. J. Fract. 132, L9-L16.

Fett, T., 2005. Influence of finite notch root radius on fracture toughness. J. Eur. Ceram. Soc. 25, 543-547.

Fett, T., 2008. Stress intensity factors, T-stresses, Weight functions. IKM 50, Universitätsverlag Karlsruhe, Karlsruhe.

Gray, H., Bannister, L.H., Berry, M.M., Williams, P.L., 1995. Gray's Anatomy: The anatomical basis of medicine & surgery. 38th ed. Churchill Livingstone.

Jelitto, H., Felten, F., Swain, M.V., Balke, H., Schneider, G.A., 2007. Measurement of the total energy release rate for cracks in PZT under combined mechanical and electrical load. J. Appl. Mech. 74, 1197-211.

Kinney, J.H., Pople, J.A., Marshall, G.W., Marshall, S.J. 2001. Collagen orientation and crystallite size in human dentin: a small angle x-ray scattering study. Calcif. Tissue Int. 69, 31-37.

Koester, K.J., Ager, J.W., Ritchie, R.O., 2008. The effect of aging on crack-growth resistance and toughening mechanisms in human dentin. Biomaterials 29, 1318-28.

Leevers, P.S., Radon, J.C., 1982. Inherent stress biaxiality in various fracture specimen geometries. Int. J. Fract. 19, 311-325.

Lussi, A., 2006. Dental erosion: From diagnosis to therapy. 1st ed. Karger, Basel.

Maas, M.C., Dumont, E.R., 1999. Built to last: the structure, function and evolution of primate dental enamel. Evol. Anthropol. 8, 133-52.

Munz, D., Fett, T., 2001. Ceramics – Mechanical properties, failure behaviour and materials selection. 2nd ed. New York: Springer.

Murakami, Y. Stress intensity factors handbook. 1st ed. Oxford: Pergamon.

Nisitani, H., Mori, K., 1985. Influence of supporting conditions on stress intensity factors for single-edge-cracked specimens under bending. Reports of the Kyushu Univ. 58, 751-755. (quoted in the handbook of Murakami et al., Vol. 1, Section 1.6).

Noda, N.A., Oda, K., 1992. Numerical solutions of the singular integral equations in the crack analysis using the body force method. Int. J. Fract. 58, 285-304.

Oesterle, L.J., Shellhart, W.C., Belanger, G.K., 1998. The use of bovine enamel in bonding studies. Am. J. Orthod. Dentofac. Orthop. 114, 514-20.

Sanches, R.P., Otani, C., Damiao, A.J., Miyakawa, W., 2009. AFM characterization of bovine enamel and dentine after acid etching. Micron 40, 502-6.

Sano, H., Ciucchi, B., Matthews, W.G., Pashley, D.H., 1994. Tensile properties of mineralized and demineralized human and bovine dentin. J. Dent. Res. 73, 1205-1211.

Schilke, R., Lisson, J.A., Bauss, O., Geurtsen, W., 2000. Comparison of the number and diameter of dentinal tubules in human and bovine dentine by scanning electron microscopic investigation. Arch. Oral. Biol. 45, 355-361.

Tada, H., Paris, P.C., Irwin, G.R., The stress analysis of cracks handbook, Del Research Corporation, 1986.
Ten Cate, AR., 2003. Oral histology - development, structure and function. 7th ed. Mosby, St Louis.